Article

Synthesis of Calcium Titanate Based on Natural Rutile from Madagascar

Tokimandimby Rakotonjanahary [1, 2]
https://orcid.org/0009-0009-5011-0527
tokimandimby.pc@gmail.com
tokimandimby@yahoo.fr

Nirina Rasolofoson [1]
https://orcid.org/0009-0009-1264-0308
nirizi.rasolofoson@gmail.com

Ravo Tokiniaina Ranaivoson [1]
https://orcid.org/0000-0003-2233-6106
tokiniainaravor13@gmail.com

Alain Gibaud [2]
https://orcid.org/0000-0002-7777-6427
alain.gibaud@univ-lemans.fr

Abstract

This study describes a solid-state synthesis method for calcium titanate derived from the purification of natural rutile from Madagascar. Purification of this raw ore with concentrated hydrochloric acid eliminated undesirable secondary phases, such as hematite and montroseite, which were detected by various analytical techniques, including X-ray diffraction, infrared spectroscopy, and Raman spectroscopy. The synthesis of $CaTiO_3$ at 1 100 °C from the purified rutile and calcium carbonate led to the formation of an orthorhombic calcium titanate, which was characterised by these advanced analytical methods. Dielectric characterisation of the synthesised $CaTiO_3$ revealed stable permittivity and low dielectric losses over a wide frequency range.

Keywords: rutile; calcium titanate; purification; solid-state reaction; characterisation; dielectric properties

1 National Institute of Nuclear Sciences and Techniques (INSTN-Madagascar).
2 Institute of Molecules and Materials of Le Mans (IMMM), Le Mans University, France.

UNISA university of south africa PRESS
Nano-Horizons
Volume 5 | 2026 | #21935 | 19 pages
https://doi.org/10.25159/3005-2602/21935
ISSN 3005-2602 (Online)

1 Introduction

Natural rutile from Madagascar is a material with potential for studying crystallographic properties, structural analysis of natural TiO_2, nanomaterial synthesis, and applications in optics and electronics. Studies have indicated that the rutile structure is the most thermodynamically stable at high temperatures (up to 2 000 K) among the TiO_2 polymorphs [1]. In other words, rutile possesses promising thermoelectric properties and potential for industrial heat recovery. Natural rutile from Madagascar could therefore serve as a raw material for the manufacture of energy materials, thermoelectric devices, and high-temperature applications [2]. Furthermore, the rutile (110)TiO_2 surface exhibits significant photocatalytic properties being studied for nitrogen fixation, pollution control, and solar energy conversion. Natural Malagasy rutile can be studied for environmental photocatalysis, nanomaterials and solar applications [3].

To our knowledge, few studies have reported the synthesis of $CaTiO_3$ directly from natural rutile ore, particularly from Malagasy mineral resources. The present work demonstrates the feasibility of transforming locally available rutile into value-added dielectric ceramics via a simple solid-state route. Obtaining high-purity rutile is essential to its use as a raw material in the manufacture of compounds such as calcium titanate ($CaTiO_3$). A purification step is therefore necessary to make it useful for the synthesis of advanced materials. Calcium titanate ($CaTiO_3$), first identified in 1839 by the German mineralogist Gustav Rose, is a perovskite-type oxide widely used in electronics and as a component of Synroc, a synthetic rock used for the containment of nuclear waste [4]. Owing to its unique dielectric, optical and structural properties, it has attracted considerable interest for its applications in microwave technologies. This material exhibits a high dielectric constant, a low loss factor and a remarkable resonant frequency temperature coefficient, making it ideal for devices such as filters, resonators and antennas [5], [6].

The solid-state reaction synthesis method was chosen to produce $CaTiO_3$. This is a conventional technique that involves mixing calcium and titanium oxides and heating the mixture to a high temperature. Achieving phase purity requires prolonged heating and a significant energy input [7].

This study uses a two-step process: first, the purification of natural rutile ore from Madagascar by acid leaching; second, the synthesis of calcium titanate by high-temperature solid-state reaction. This approach allows the direct use of purified natural rutile as a source of titanium and calcium carbonate [8], reducing production costs and promoting the local valorisation of Malagasy mineral resources.

2 Experimental Details

Natural rutile was first mechanically ground into a fine powder to facilitate subsequent purification. Chemical purification of this powder was carried out with 37% concentrated hydrochloric acid at a solid-to-liquid ratio of 1:10 (g/mL). The resulting

suspension was stirred magnetically at 500 rpm and maintained at a constant temperature of 70 °C for 3 hours. After the reaction, the suspension was cooled to room temperature and then filtered under vacuum using a Büchner funnel. The residue was thoroughly washed with distilled water to neutrality to remove all traces of acid. The purified solid was then dried in a ventilated oven at 70 °C for 2 hours.

For comparison, a reference rutile sample was prepared by thermal conversion of commercial anatase (Alfa Aesar) by calcination. Anatase powder was placed in a muffle furnace and heated to 900 °C at a rate of 5 °C/min, then held at this temperature for 8 hours under ambient air [9].

Purified rutile was used as a titanium source for the synthesis of calcium titanate. Calcium carbonate served as the calcium precursor. The reagents were mixed in equimolar proportions and manually ground in an agate mortar for 30 minutes. The formation of $CaTiO_3$ results from a solid-state reaction between titanium dioxide and calcium carbonate. Upon calcination, calcium carbonate thermally decomposes at 700 °C according to the following process [10], [11]:

$$CaCO_{3(s)} + TiO_{2(s)} \xrightarrow{1100°C} CaTiO_{3(s)} + CO_{2(g)} \quad (1)$$

$$CaCO_{3(s)} \xrightarrow{700°C} CaO_{(s)} + CO_{2(g)} \quad (2)$$

The calcium oxide formed then reacts with titanium dioxide at high temperature to form calcium titanate according to the following overall equation [8]:

$$CaO_{(s)} + TiO_{2(s)} \xrightarrow{1100°C} CaTiO_{3(s)} \quad (3)$$

This reaction requires a sufficient activation temperature to allow the diffusion of solid species and the growth of the perovskite phase. The mixture was then placed in a porcelain crucible and calcined in a kiln at 1 100 °C for 8 hours, with a heating rate of 5 °C/min. After air cooling, the product was washed successively with distilled water and then treated with a dilute solution of acetic acid. Dielectric measurements were performed using a broadband dielectric spectrometer (Novocontrol Technologies' Alpha-A High Performance Frequency Analyzer), which operates in the frequency range of 0.1 Hz to 10^7 Hz. These measurements were carried out at temperatures of 20 °C, 40 °C, 80 °C and 100 °C under ambient conditions. Before the measurements, the synthesised $CaTiO_3$ powder was pressed into circular pellets 10 mm in diameter and approximately 0.71 mm thick using a uniaxial hydraulic press under a pressure of 5 tonnes. The pellets were then sintered at 1 100 °C for 8 hours to improve their densification. To ensure good electrical contact and minimise electrode polarisation effects, both faces of the ceramic pellets were coated with conductive gold electrodes by dry pressing fine gold powder.

The electrode surface area was precisely controlled, and the sample thickness was measured using a digital micrometer before dielectric characterisation. The complex permittivity ($\varepsilon^* = \varepsilon' - j\varepsilon''$) was obtained directly from the measured capacitance and dielectric loss using the instrument's software. To quantitatively analyse the material's behaviour as a function of frequency, the experimental data for ε' and ε'' were fitted to the Cole–Cole model [12] according to equations (4)–(7), using Python software containing the matplotlib, numPy, and sciPy libraries, with custom functions defined for the real and imaginary components of the complex permittivity.

$$\varepsilon^*(\omega) = \varepsilon'(\omega) + j\varepsilon''(\omega) = \varepsilon_\infty + \frac{\varepsilon_s - \varepsilon_\infty}{1 + (j\omega\tau)^{1-\alpha}} \tag{4}$$

$$\varepsilon'(\omega) = \varepsilon_\infty + \frac{(\varepsilon_s - \varepsilon_\infty)[1 + R\cos\theta]}{[1 + 2R\cos\theta + R^2]} \tag{5}$$

$$\varepsilon''(\omega) = \frac{(\varepsilon_s - \varepsilon_\infty) R\sin\theta}{[1 + 2R\cos\theta + R^2]} \tag{6}$$

$$R = (\omega\tau)^{1-\alpha} \text{ and } \theta = \frac{\pi}{2}(1-\alpha) \tag{7}$$

where ε_S is the static permittivity, ε_∞ the high-frequency permittivity, $\omega = 2\pi f$ the angular frequency, τ the relaxation time and α the distribution parameter ($0 \leq \alpha < 1$).

3 Results and Discussion

3.1 Characterisation of Rutile

X-ray diffraction (XRD) analysis in Figure 1(a) revealed that the dominant crystalline phase is rutile TiO_2 (approximately 73.92%), accompanied by secondary phases identified as hematite (Fe_2O_3, approximately 4.97%) and montroseite ($VO(OH)_2$, approximately 21.09%). These results confirm the multiphase nature of the natural ore. After purification, the Rietveld-refined X-ray diffractogram of the purified rutile in Figure 1(b) revealed characteristic peaks at angles 2θ corresponding to the crystallographic planes, therefore confirming the exclusive presence of the rutile phase [13]. The absence of secondary signals testifies to the effectiveness of the acid treatment in eliminating unwanted phases. Rietveld refinement confirmed a tetragonal structure in Figure 2 with space group $P4_2/mnm$, characteristic of rutile. The lattice parameters of this rutile phase are a = 4.5995 Å and c = 2.9627 Å [14]. The Rietveld refinement is presented in Tables 1 and 2.

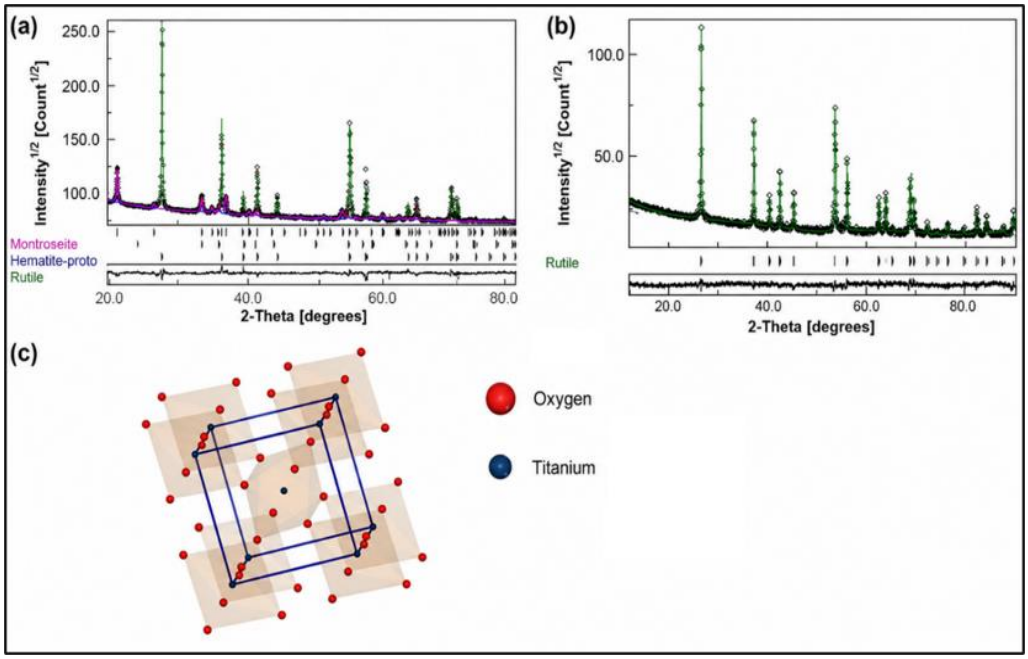

Figure 1: (a) X-ray diffraction pattern of natural rutile; (b) X-ray diffraction pattern of purified rutile; (c) tetragonal structure of purified rutile

Table 1: Lattice parameters of purified rutile after Rietveld refinement

Crystal system	Space group	a (Å)	b (Å)	c (Å)	Cell volume (Å³)	Crystallite size (Å)	Microstrain (ε)
Tetragonal	$P4_2/mnm$	4.5995	4.5995	2.9626	62.6758	1 889.09	4.822×10^{-4}

Rwp (%) = 8.4053; Rb (%) = 6.3909; Rexp (%) = 5.7880

Table 2: Rietveld analysis of atomic positions in purified rutile

Atom	Oxidation state	Wyckoff position	x	y	z	Biso (Å²)	Occupancy
Ti	+4	2a	0	0	0	0.01270	1
O1	−2	4f	0.3033	0.3033	0	0.4723	1
O2	−2	4f	0.3033	0.3033	0	0.4723	1

For natural rutile in Figure 1(a), characteristic Ti-O stretching vibrations were observed between 500 and 750 cm^{-1}, corresponding well to the rutile structure [15]. An additional absorption band, located between 950 and 1 025 cm^{-1}, was attributed to montroseite,

confirming the presence of vanadium-containing impurities [16]. Broad bands between 3 000 and 3 400 cm^{-1} were associated with adsorbed water, indicating the presence of surface hydroxyl groups [17]. Overall, these results indicate that the raw ore is primarily composed of TiO_2 in the form of rutile, but contains significant amounts of iron and vanadium impurities. For purified rutile, the Fourier transform infrared spectroscopy (FTIR) spectrum in Figure 2(b) shows stretching bands characteristic of Ti-O-Ti bonds, particularly around 500 cm^{-1} and 700 cm^{-1}, and a band around 1 630 cm^{-1} associated with the adsorption of water molecules (δHOH) on the surface [13], [18]. Furthermore, the signals corresponding to V-O bonds around 950–1 025 cm^{-1} have disappeared, indicating efficient rutile purification.

Raman spectroscopy in Figure 2(c) confirmed the rutile structure of titanium dioxide, revealing characteristic peaks around 143, 240, 450 and 610 cm^{-1}.

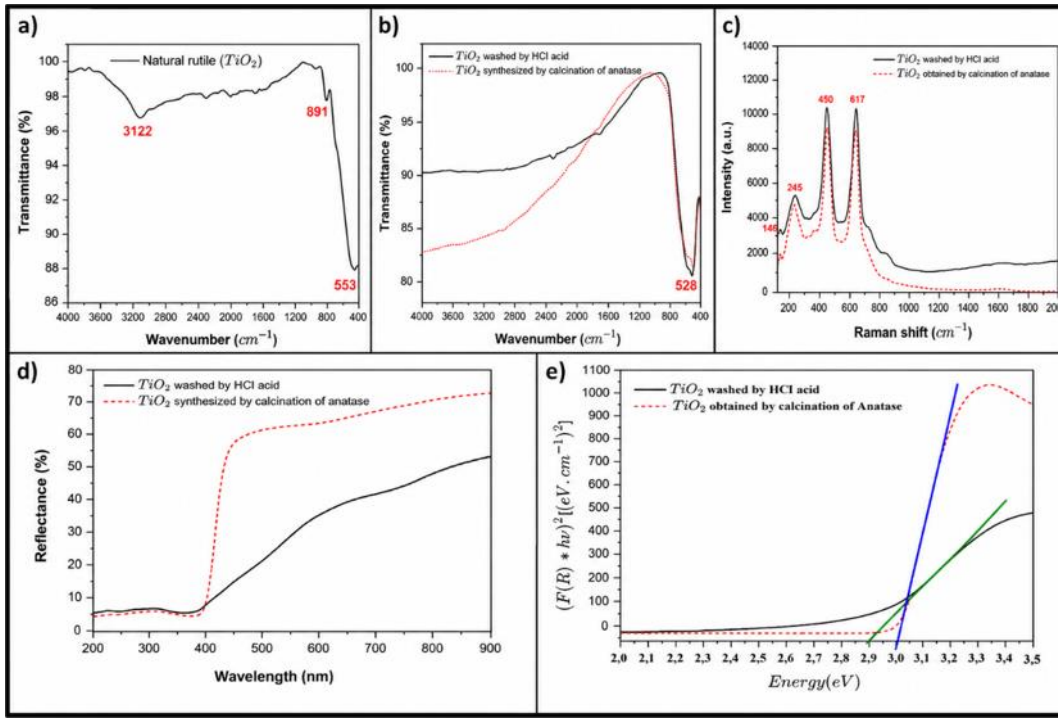

Figure 2: (a) IR spectrum of natural rutile; (b) IR spectrum of purified rutile; (c) Raman spectrum of purified rutile; (d) UV-Vis reflectance spectrum rutile; (e) determination of band gap energy of rutile by the Tauc method

Titanium dioxide, in the form of rutile, has a tetragonal crystal structure belonging to the space group $P4_2/mnm$. Analysis of its vibrational properties, based on group theory,

allows us to identify the normal vibrational modes at the centre of the Brillouin zone, represented by the following expression:

$$\Gamma_{vibration} = A_{1g} + A_{2g} + A_{2u} + B_{1g} + B_{1u} + B_{2g} + E_g + 2E_u \qquad (8)$$

Among these modes, only three are infrared active: the A_2u mode and two Eu modes. The others are Raman active or optically inactive. The A_2u and Eu modes involve relative displacements between the Ti^{4+} cations and the O^{2-} anions, inducing variations in the dipole moment necessary for the absorption of infrared radiation.

The A_2u mode corresponds to a polar longitudinal vibration along the c-axis, while the two Eu modes are degenerate and manifest as vibrations in the plane perpendicular to this axis. These corresponding absorption bands generally appear in the 235 – 450 cm^{-1} region for Eu modes, and around 500–700 cm^{-1} for the A_2u mode [15]. These spectral features constitute a vibrational signature of rutile.

In Raman spectroscopy, only vibrational modes that induce a change in the polarisability of the crystal lattice are active. Among the vibrational modes decomposed according to group theory, only the A_1g, B_1g, B_2g and Eg modes are Raman active [19], [20]. The Eg mode is associated with symmetrical bending vibrations in the basal plane, while the A_1g mode corresponds to symmetrical stretching vibrations of oxygen atoms along the c-axis. The B_1g and B_2g modes correspond to angular deformations of oxygen atoms [21]. Moreover, these results agree with the spectra published for titanium dioxide in the form of rutile, obtained by thermal transformation of anatase at 900 °C [22].

The UV-Vis absorption spectrum (Figure 2(d)) of the purified rutile shows strong absorption in the ultraviolet region, with an abrupt absorption edge around 400 nm. The Tauc method was used to estimate the band gap energy of the purified rutile. The reflectance was transformed into an absorption coefficient using the Kubelka–Munk function:

$$F(R) = \frac{(1-R)^2}{2R} \qquad (9)$$

$$(Fh\nu)^n = B(h\nu - E_g) \qquad (10)$$

Where R represents the reflectance and B is a constant characteristic of the material. Then, $(F*h\nu)^2$ was plotted as a function of the photon energy . The value of $n = 2$ corresponds to a direct band gap transition [23]. The linear portion was extrapolated to $(F*h\nu)^2 = 0$. The intersection of the line with the abscissa axis provides an estimate of the band gap energy. The analysis of the UV-Vis spectrum by the Tauc method in

Figure 2(e) allowed evaluating the band gap width of the purified rutile at around 3.00 eV [24], [25].

Scanning electron microscopy (SEM) in Figure 3(a) of the natural rutile powder revealed a heterogeneous morphology with an average particle size of approximately 8.25 µm. In contrast, the morphology of the purified rutile particles revealed a relatively homogeneous particle size distribution, with irregularly shaped particles and an average size of approximately 3.87 µm.

Energy-dispersive X-ray spectroscopy (EDX) analysis in Figure 3(b) confirmed the presence of titanium and oxygen as the major elements, corresponding to the TiO_2 composition of the sample. However, traces of iron, silicon and vanadium were also detected, indicating the presence of mineral impurities in the raw material. After purification, the EDX results showed a significant decrease in undesirable elements such as iron, silicon and especially vanadium, indicating effective removal of impurities through hydrochloric acid treatment.

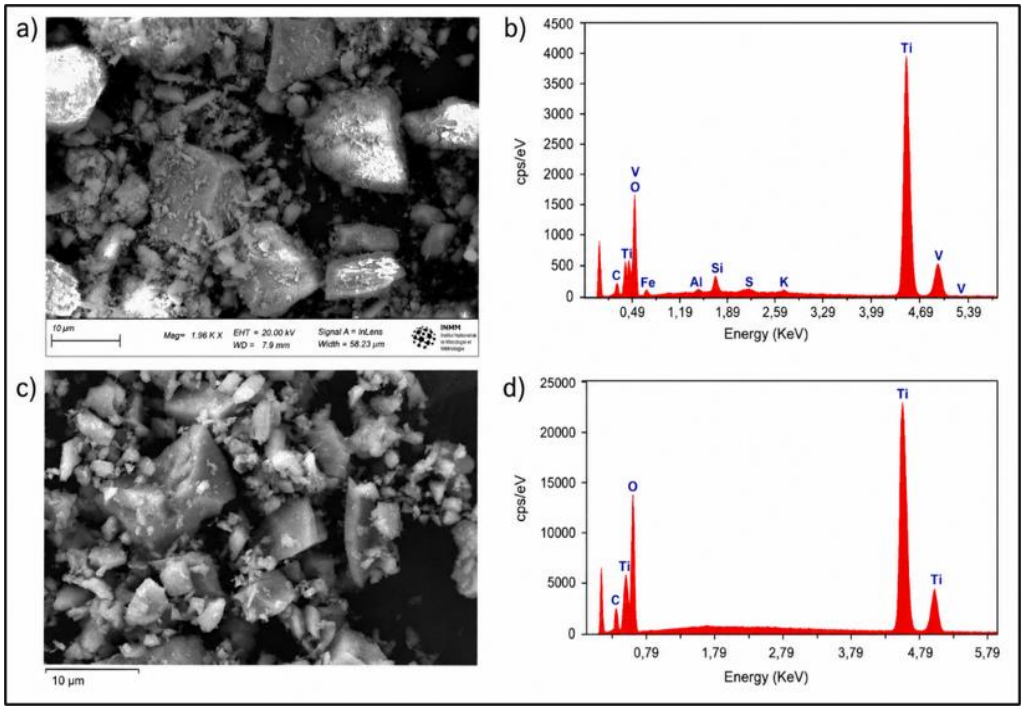

Figure 3: (a) SEM images of natural rutile; (b) EDX analysis of raw natural rutile; (c) SEM images of the purified rutile; (d) EDX spectra of the purified natural rutile

3.2 Characterisation of the Synthesised Calcium Titanate

X-ray diffraction analysis of the synthesised CaTiO3 in Figure 4(a) reveals that the dominant crystalline phase is calcium titanate ($CaTiO_3$), with a calculated content of approximately 98.88%. Minor secondary peaks corresponding to rutile TiO_2 are also observed, notably around $2\theta = 27.40°$ and 36.23°, representing approximately 1.12% of the crystalline composition. These residual peaks indicate a slight incomplete transformation of the TiO_2 precursor during synthesis.

The XRD pattern corresponds well to that expected for the orthorhombic structure of $CaTiO_3$, as indicated in the references [4], [10] and [26] and in Figure 4(b). The lattice parameters determined for the $CaTiO_3$ phase are a = 5.3851 Å, b = 5.4429 Å and c = 7.6457 Å [26]. Detailed crystallographic information, including lattice parameters and atomic positions obtained by Rietveld refinement, is summarised in Tables 3 and 4.

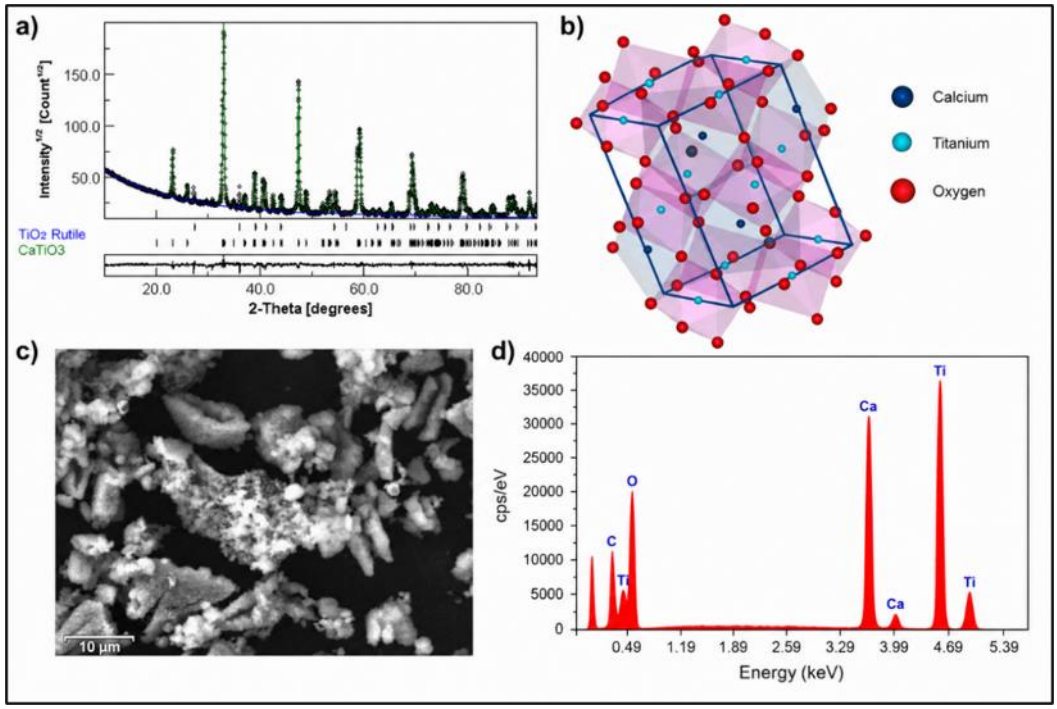

Figure 4: (a) XRD diagram of calcium titanate; (b) orthorhombic structure of synthesised calcium titanate obtained on VESTA; (c) SEM image of the synthesised calcium titanate; (d) EDX spectra of calcium titanate

Figure 4(c) shows SEM images revealing agglomerated particles with irregular morphology. The typical particle size is approximately 9.02 µm. Energy dispersive X-ray spectroscopy (Figure 4(d)) confirms the presence of calcium (Ca), titanium (Ti) and

oxygen (O), with an atomic Ca/Ti ratio close to 1 consistent with the stoichiometric composition of $CaTiO_3$. Additional elements detected, such as iron (Fe), silicon (Si), sulfur (S) and aluminium (Al), are attributed to impurities originating from the rutile precursors used in the synthesis.

Table 3: Rietveld refinement of the lattice parameters of synthesised $CaTiO_3$

Crystal system	Space group	a (Å)	b (Å)	c (Å)	Cell volume (Å³)	Crystallite size (Å)	Microstrain (ε)
Orthorhombic	Pbnm	5.3851	5.4428	7.6457	224.10	3 203.26	7.9564×10^{-4}

Rwp (%) = 6.2802; Rb (%) = 4.2616; Rexp (%) = 3.2114

Table 4: Rietveld refinement of the atomic positions of the synthesised $CaTiO_3$

Atom	Oxidation state	Wyckoff position	x	y	z	Biso (Å²)	Occupancy
Ca	+2	4c	0.9933	0.0348	0.25	0.3580	1
Ti	+4	4b	0.5	0	0	0.1509	1
O1	−2	4c	0.0717	0.4833	0.25	0.0921	1
O2	−2	8d	0.7097	0.2911	0.0365	0.0568	1

The FTIR analysis in Figure 5(a) revealed the characteristic vibrational modes of the $CaTiO_3$ crystal lattice. The absorption bands observed between 500 and 600 cm^{-1} are associated with Ti-O bond stretching vibrations, while those between 800 and 900 cm^{-1} are related to Ca-O bond valence vibrations. The bands between 250 and 500 cm^{-1} correspond to Ti-O-Ti angular deformation vibrations. In this crystal structure, group theory analysis predicts a total of 25 infrared-active vibrational modes, distributed according to irreducible representations.

$$\Gamma_{vibration} = 9B_{1u} + 7B_{2u} + 9B_{3u} \quad (11)$$

These modes are primarily associated with the internal vibrations of the TiO_6 octahedra and the translations of the Ca^{2+} and Ti^{4+} ions. The B_1u modes correspond to asymmetric stretching vibrations of Ti-O bonds in the 500–750 cm^{-1} region, while the B_3u modes correspond to Ti-O-Ti angular strain vibrations in the 250–500 cm^{-1} range.

The B_1u modes are related with octahedral vibrations of TiO_6 at frequencies between 800 and 900 cm^{-1} [27]. These results are consistent with previous studies on the characteristic vibrations of the $CaTiO_3$ perovskite structure [7].

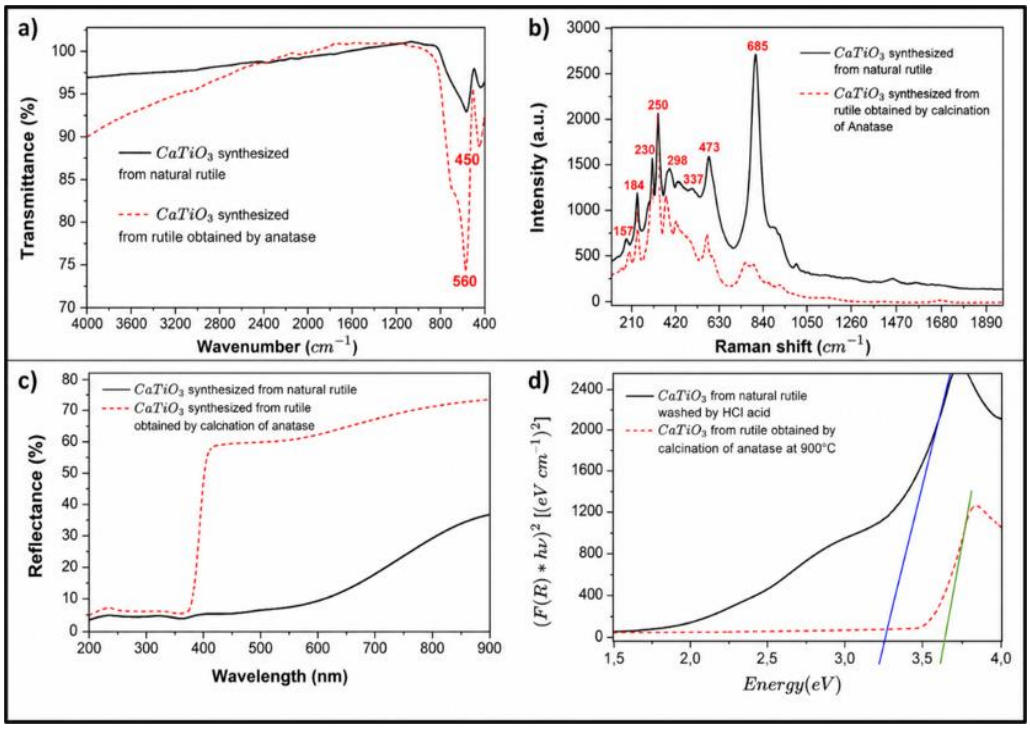

Figure 5: (a) IR spectra of synthesised calcium titanate; (b) Raman spectrum of synthesised calcium titanate at 1 100 °C; (c) UV-Vis reflectance spectrum of the synthesised calcium titanate; (d) determination of the band gap energy of $CaTiO_3$ by the Tauc method

The Raman spectrum of $CaTiO_3$ in Figure 5(b) shows characteristic peaks in the 150–750 cm^{-1} range. Among the most characteristic modes are those around 157, 184, 230, 250, 298, 337, 473 and 685 cm^{-1}, associated with Ca-O vibrations and octahedral rotations of TiO_6. The modes between 320 and 530 cm^{-1} correspond mainly to bending and stretching vibrations of the Ti-O bonds, while the higher frequencies, from 580 to 750 cm^{-1} are attributed to symmetric and asymmetric internal vibrations of the TiO_6 octahedron. These results are consistent with published data for $CaTiO_3$, confirming the formation of the perovskite structure [28], [29], [30].

The UV-Vis diffuse reflectance spectrum of pure calcium titanate in Figure 5 (c) shows an absorption edge around 380 nm. Applying the Tauc method with the Kubelka–Munk function $F = (k\alpha)^2/2s$, where $k\alpha$ is the absorption coefficient, s is the scattering coefficient, and hν is the photon energy, we were able to determine the value of $n = 2$ corresponds to a band gap transition [24], [29]. From this analysis, we estimated that the band gap energy of the synthesised calcium titanate is around 3.3 eV in Figure 5(d). This value is consistent with the data reported in the literature for calcium titanate [31].

The UV-Vis diffuse reflectance spectra of the $CaTiO_3$ samples synthesised from natural rutile and from rutile obtained by anatase calcination display optical behaviours typical of perovskite materials based on titanate, further confirming the successful synthesis of the desired compound.

3.3 Dielectric Characterisation of Calcium Titanate

The strong dielectric dispersion observed at low frequencies is explained by the Maxwell–Wagner interfacial polarisation mechanism. According to this model, the ceramic consists of semiconductor grains separated by highly resistive grain boundaries [32]. In polycrystalline $CaTiO_3$ ceramics, the grains are relatively conductive while the grain boundaries are more resistive. Under the influence of an applied electric field, charge carriers accumulate at grain boundaries, inducing space charge polarisation and, consequently, high dielectric permittivity at low frequencies. As the frequency increases, the charge carriers can no longer keep pace with the rapid oscillation of the electric field [33]. The interfacial polarisation then gradually decreases, leading to a reduction in both the real and imaginary parts of the permittivity. This behaviour is characteristic of heterogeneous dielectric materials and confirms the contribution of grain boundary effects to the dielectric relaxation process [34].

Figure 6(a) illustrates the frequency dependence of the real part of the dielectric permittivity of $CaTiO_3$ synthesised at 20 °C. These experimental data reveal a decrease in ε' as the frequency increases. At low frequencies (≈ 0.1–10 Hz), the permittivity (ε') reaches a maximum value of approximately 125. The dipoles then have sufficient time to align with the applied field, inducing a strong polarisation (ε'), reflecting the full response of slower polarisation mechanisms with α, an ε' parameter of approximately 0.15. In contrast, at high frequencies (> 10^4 Hz), ε' converges to a stable value. The high-frequency permittivity, of approximately 75, indicates the high-frequency permittivity limit beyond which the dipoles can no longer synchronise with the oscillating electric field. The transition region (≈ 1–10^4 Hz) reveals the dielectric relaxation of the material. This model reproduces empirical data, suggesting a non-ideal relaxation process characterised by a relaxation time distribution around 0.5 s. This behaviour demonstrates that $CaTiO_3$ possesses relaxer-like dielectric properties, positioning it as a high-permittivity ceramic material suitable for applications in electronic components such as multilayer ceramic capacitors.

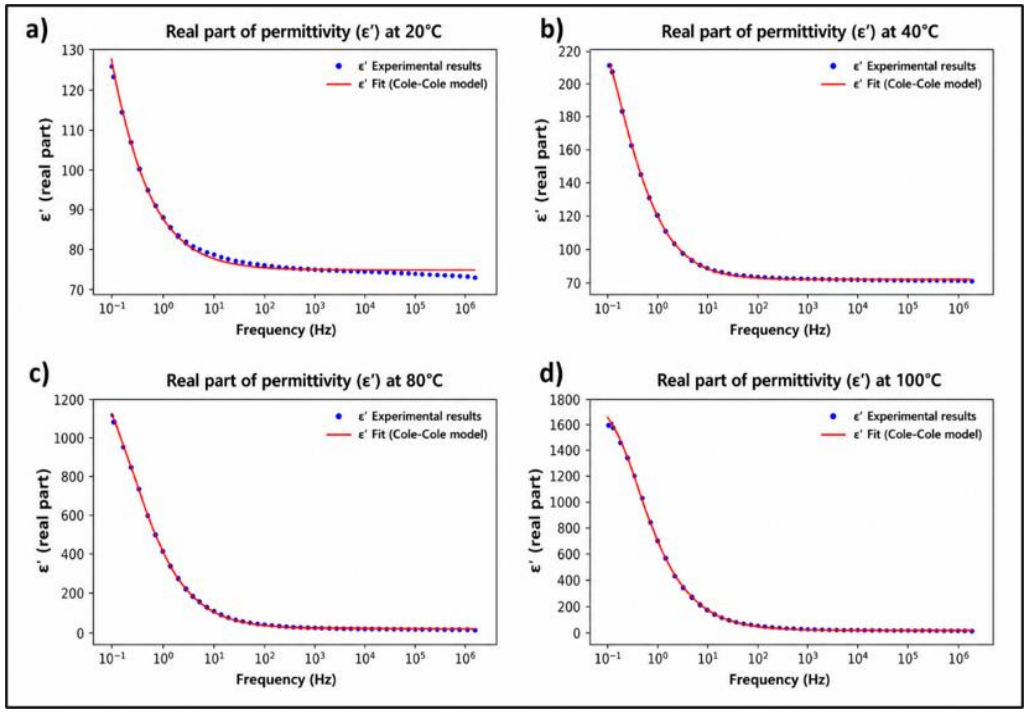

Figure 6: (a) Fit of eps' for $CaTiO_3$ at 20 °C according to the Cole–Cole model; (b) fit for eps" of $CaTiO_3$ at 20 °C according to the Cole–Cole model; (c) fit of eps' for $CaTiO_3$ at 40 °C according to the Cole–Cole model; (d) fit for eps" of $CaTiO_3$ at 40 °C according to the Cole–Cole model

The frequency-dependent behaviour in Figure 7(a) of the imaginary part of the dielectric permittivity (ε″) of $CaTiO_3$ at 20 °C was analysed to investigate the dielectric loss characteristics of the material. These data reveal that ε″ exhibits high values (~80) at low frequencies (≈ 0.1 Hz), indicating significant energy dissipation, generally attributed to interfacial polarisation or charge carrier mobility. At mid-frequencies (≈ 1 Hz to 10^4 Hz), the permittivity decreases sharply, reflecting dielectric relaxation. This means that the material's response no longer follows the applied field, which is characteristic of a relaxation process in polarisable materials. As the frequency increases (> 10^5 Hz), ε″ is very small (close to zero), losses are negligible, and the material therefore no longer accurately follows rapid changes in the field. The Cole–Cole model fits the experimental data well. At high frequencies, the imaginary part tends towards zero, indicating minimal losses, as the polarisation mechanisms cannot keep pace with the rapid change in the external field. These results demonstrate the complex dielectric behaviour of $CaTiO_3$, characterised by a strong frequency dependence. The other results obtained from this Cole–Cole fitting model for temperatures of 40 °C, 80 °C and 100 °C are also important. Table 5 summarises the evolution of dielectric losses and relaxation

behaviour as a function of temperature, highlighting changes in loss amplitude, relaxation time and position of the loss peak.

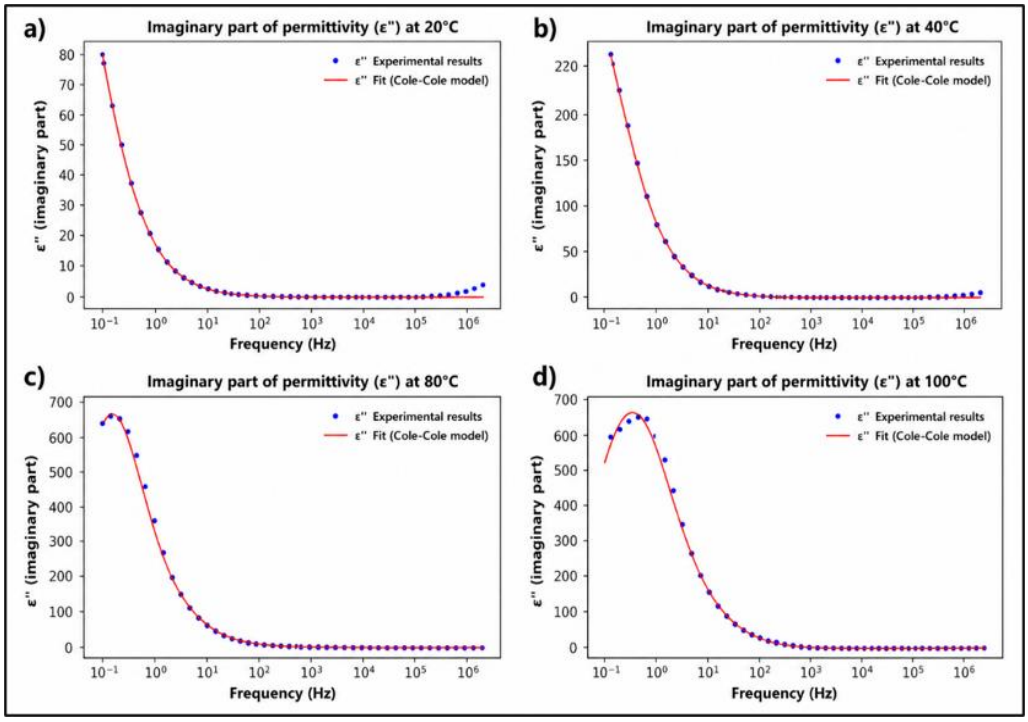

Figure 7: (a) Fit of eps' for $CaTiO_3$ at 80 °C according to the Cole–Cole model; (b) fit for eps" of $CaTiO_3$ at 80 °C according to the Cole–Cole model; (c) fit of eps' for $CaTiO_3$ at 100 °C according to the Cole–Cole model; (d) fit for eps" of $CaTiO_3$ at 100 °C according to the Cole–Cole model

Table 5: Evolution of the parameters of the Cole–Cole model (ε_s, ε_∞, τ) as a function of the temperature of $CaTiO_3$

Temperature (°C)	εs	ε∞	τ (s)	α
20	125.187	77.337	0.452	0.08
40	216.754	77.016	0.558	0.11
80	1098.600	29.270	0.492	0.18
100	1597.500	36.610	0.236	0.24

Table 6 compares the dielectric properties of the synthesised $CaTiO_3$ with previously reported $CaTiO_3$ ceramics prepared by different synthesis methods reported in the literature.

Table 6: Comparative table of the dielectric properties of $CaTiO_3$ from the literature

References	Synthesis method	Frequency	Temperature	ε′ (dielectric constant)	Main dielectric behaviour
[35]	Solid-state reaction	1 kHz	Room temperature	~150	Grain-boundary and Maxwell–Wagner relaxation
[36]	Solid-state reaction	1 kHz	Room temperature	~ 180	Non-Debye relaxation
[37]	Nanocrystalline ceramic	100 Hz–1 MHz	Room temperature	High ε′ at low frequency	Grain boundary effect
[38]	Plasma spray	100 Hz–1 MHz	Room temperature	Stable ε′	Low dielectric loss
Present work	Natural rutile solid-state reaction	0.1 Hz–10^7 Hz	20–100 °C	125–1 597	Maxwell–Wagner relaxation

The dielectric permittivity of the $CaTiO_3$ obtained in this work is comparable to values reported for synthesised by conventional methods in the solid state. According to the Maxwell–Wagner model, the strong dielectric response observed at low frequencies is primarily attributed to interfacial polarisation effects related to grain boundaries. Compared with chemically synthesised precursors reported in the literature, the present approach demonstrates that natural Malagasy rutile can be successfully used as a low-cost precursor for dielectric $CaTiO_3$ ceramics while maintaining competitive dielectric properties.

4 Conclusion

From natural rutile from Madagascar, calcium titanate ($CaTiO_3$) was successfully synthesised by a solid-state reaction method. Rutile was purified through a combination of chemical and thermal treatments, effectively removing impurities and resulting in high purity TiO_2 powder. X-ray diffraction analysis confirmed the orthorhombic crystal structure of the synthesised $CaTiO_3$, with lattice parameters consistent with published reference data [4], [24]. Infrared spectroscopy revealed the characteristic vibrational modes of Ti–O and Ca–O bonds, confirming the formation of the perovskite structure. Raman spectroscopy identified vibrational modes associated with TiO_6 octahedra and Ca^{2+} cations corroborating the crystalline nature of $CaTiO_3$.

Dielectric characterisation demonstrated a significant increase in static permittivity with temperature, indicating increased dipolar polarisation, while relaxation time decreased, confirming a thermally activated relaxation process. These results highlight the potential of the synthesised $CaTiO_3$ for applications in solar cells [39], capacitors [35], [37], and

catalysts [26]. From the point of view of experimental conditions, the calcination temperature plays a crucial role in the formation of the perovskite phase.

Looking forward to the future, an in-depth study of the electrical, optical and magnetic properties of $CaTiO_3$ would provide valuable information for its technological applications. The solid-state synthesis method used here is economical and allows for precise control of the composition [38], [40]. This study on the synthesis of calcium titanate from Malagasy rutile opens promising prospects for the economic and technological development of Madagascar. By using mineral resources locally, particularly raw rutile transformed into high value-added materials such as $CaTiO_3$, Madagascar could create jobs and stimulate its economy. Given the potential of calcium titanate in solar cells and photocatalysis [39], [41], investing in the research and development of renewable energy applications is therefore strongly recommended.

5 References

[1] J. R. Trail, B. Monserrat, P. López Ríos, R. Maezono and R. J. Needs, "Quantum Monte Carlo Study of the energetics of the rutile, anatase, brookite, and columbite TiO_2 polymorphs," *Phys. Rev. B*, vol. vol. 95, p. 121108(R), Mar. 2017, doi: 10.1103/Phys Rev B.95.121108.

[2] S. Thébaud, Ch. Adessi and G. Bouzerar, "Investigating the high-temperature thermoelectric properties of *n*-type rutile TiO_2," *Phys. Rev. B*, vol. 100, p. 195202, Nov. 2019, doi: 10.1103/Phys Rev B.100.195202.

[3] B. M. Comer and A. J. Medford, "Analysis of Photocatalytic Nitrogen Fixation on Rutile TiO_2 (110)," 2018, https://arxiv.org/abs/1707.03031v3.

[4] L. S. Cavalcante *et al*., "Synthesis, structural refinement and optical behavior of $CaTiO_3$ powders: A comparative study of processing in different furnaces," *Chem. Eng. J.*, vol. 143, no. 1, pp. 299–307, Sept. 2008. doi: 10.1016/j.cej.2008.05.017.

[5] Z. Ming, K. Zhao and Y. Huang, "Influence of different Milling Process on the properties of $CaTiO_3$-$NdAlO_3$ Dielectric Ceramics and its Microwave Devices," *IOP Conf. Ser.: Mater. Sci. Eng.*, vol. 1043, Jan. 2021, doi: 10.1088/1757-899X/1043/5/052002.

[6] C.-L. Huang, J.-Y. Chen and G.-S. Huang, "A new low-loss dielectric using $CaTiO_3$-modified $(Mg_{0.95}Mn_{0.05})TiO_3$ ceramics for microwave applications," *J. Alloys Comp*., vol. 499, no. 1, pp. 48–52, Jun. 2010, doi: 10.1016/j.jallcom.2010.01.014.

[7] N. Vijayakumar *et al*., "Synthesis and characterization of calcium and magnesium based oxides and titanates for photocatalytic degradation of rhodamine B: A comparative study," *Sci. Rep.*, vol. 13, Mar. 2023, doi: 10.1038/s41598-023-30013-3.

[8] V. M. Vukotić, N. Radojević, L. Živković, Z. Vuković and B. D. Stojanović, "Mechanically Activated Synthesis of $CaTiO_3$ from Mixture of CaO and TiO_2," *MSF*, vol. 494, pp. 393–398, Sept. 2005, doi: 10.4028/www.scientific.net/msf.494.393.

[9] K. Hwang *et al*., "Fine size-regulation of nanocrystalline anatase-TiO_2via sol-gel synthesis and subsequent phase transformation by calcination," *New J. Chem.*, vol. 37, no. 5, p. 1378, Jan. 2013, doi: 10.1039/c3nj41170b.

[10] I. Hanif and H. Wiinikka, "Calcination of $CaCO_3$ and the Subsequent Sintering/Densification of CaO Directly Visualized with In-Situ SEM," *Mater. Chem. Phys.*, vol. 356, p. 132296, 2026, doi: 10.1016/j.matchemphys.2026.132296.

[11] S. K. AbdulKareem and S. A. Ajeel, "Effect of annealing temperatures on the structural and crystalline properties of $CaTiO_3$ powder synthesized via conventional solid-state method," *Mater. Today Proc.*, vol. 42, no. 5, pp. 2674–2679, Jan. 2021, doi: 10.1016/j.matpr.2020.12.647.

[12] K. S. Cole and R. H. Cole, "Dispersion and Absorption in Dielectrics I. Alternating Current Characteristics," *J. Chem. Phys*., vol. 9, no. 4, pp. 341–351, Apr. 1941, doi: 10.1063/1.1750906.

[13] S. Bhullar, S. Gupta and N. Goyal, "Investigating TiO_2 at two different calcination temperatures," *AIP Conf. Proc.*, vol. 2220, p. 20065, Jan. 2020, doi:10.1063/5.0001662.

[14] S. Murugesan, P. Kuppusami and E. Mohandas, "Rietveld X-ray diffraction analysis of nanostructured rutile films of titania prepared by pulsed laser deposition," *Mater. Res. Bull.*, vol. 45, no. 1, pp. 6–9, Jan. 2010, doi: 10.1016/j.materresbull.2009.09.012.

[15] J. F. Arcila and A. F. Hincapié, "Structural characterization of mineral with rutile inclusions (TiO_2) and manganocolumbite ($MnNb_2O_6$) by means of X-ray," *J. Phys. Conf. Ser.*, vol. 466, Nov. 2013, doi: 10.1088/1742-6596/466/1/012024.

[16] P. B. C. Forbes and J. Dubessy, "Characterization of fresh and altered montroseite [V, Fe]OOH. A discussion of alteration processes," *Phys. Chem. Minerals*, vol. 15, pp. 438–445, May 1988, doi: 10.1007/bf00311122.

[17] M. Pentrák, V. Bizovská and J. Madejová, "Near-IR study of water adsorption on acid-treated montmorillonite," *Vib. Spectrosc.*, vol. 63, pp. 360–366, Nov. 2012, doi: 10.1016/j.vibspec.2012.07.012.

[18] M. Ocaña and C. J. Serna, "Variations of the infrared powder spectra of TiO_2 and SnO_2 (rutile) with polarization," *Spectrochim. Acta A Mol. Spectrosc.*, vol. 47, no. 6, pp. 765–774, Jan. 1991, doi: 10.1016/0584-8539 (91)80148-c.

[19] F. Matossi, "The Vibration Spectrum of Rutile," *J. Chem. Phys.*, vol. 19, pp. 1543–1546, Dec. 1951, doi: 10.1063/1.1748119.

[20] Y. Huang and F. H. Pollak, "Raman investigation of rutile RuO_2," *Solid State Commun.*, vol. 43, no. 12, pp. 921–924, Sept. 1982, doi: 10.1016/0038-1098 (82)90930-9.

[21] U. Balachandran and N. G. Eror, “Raman Spectra of Titanium Dioxide,” *J. Solid State Chem.*, vol. 42, no. 3, pp. 276–282, 1982, doi: 10.1016/0022-4596(82)90006-8.

[22] T. Mazza *et al*., “Raman spectroscopy characterization of TiO_2 rutile nanocrystals,” *Phys. Rev. B*, vol. 75, Jan. 2007, doi: 10.1103/PhysRevB.75.045416.

[23] N. Ghobadi, “Band gap determination using absorption spectrum fitting procedure,” *Int. Nano Lett.*, vol. 3, no. 1, Dec. 2013, doi: 10.1186/2228-5326-3-2.

[24] T. Sekiya, M. Igarashi, S. Kurita, S. Takekawa and M. Fujisawa, “Structure dependence of reflection spectra of TiO_2 single crystals,” *J. Electron. Spectrosc. Rel. Phenom.*, vol. 92, nos 1–3, pp. 247–250, May 1998, doi: 10.1016/s0368-2048 (98)00130-3.

[25] U. Gesenhues, “The effects of plastic deformation on band gap, electronic defect states and lattice vibrations of rutile,” *J. Phys. Chem. Solids*, vol. 68, no. 2, pp. 224–235, Feb. 2007, doi: 10.1016/j.jpcs.2006.10.014.

[26] M. Sindhu, N. Ahlawat, S. Sanghi, A. Agarwal, R. Dahiya and N. Ahlawat, “Rietveld refinement and impedance spectroscopy of calcium titanate,” *Curr. Appl. Phys.*, vol. 12, no. 6, pp. 1429–1435, Nov. 2012, doi: 10.1016/j.cap. 2012.03.034.

[27] C. H. Perry, B. N. Khanna and G. Rupprecht, “Infrared studies of perovskite titanates,” *Phys. Rev.*, vol. 135, no. 2A, pp. A408–A412, Jul. 1964, doi: 10.1103/PhysRev.135.A408.

[28] Y. Wang, W. Zhong, C. Wang and P. Zhang, “First principles study on the optical properties of cubic $CaTiO_3$,” *Phys. Lett. A*, vol. 291, nos 4–5, pp. 338–342, Dec. 2001, doi: 10.1016/s0375-9601(01)00735-6.

[29] Y. X. Wang, W. L. Zhong, C. L. Wang and P. L. Zhang, “Electronic structure and properties in perovskite $CaTiO_3$ from first principle,” *Ferroelecctrics*, vol. 259, no. 1, pp. 127–132, Oct. 2011, doi: 10.1080/00150190108008728.

[30] U. Balachandran and N. G. Eror, “Laser-induced Raman scattering in calcium titanate,” *Solid State Comm.*, vol. 44, no. 6, pp. 815–818, Nov. 1982, doi: 10.1016/0038-1098 (82)90280-0.

[31] M. Tsabit Ayman *et al.*, “Direct Hydrothermal Synthesis of Low-Bandgap $CaTiO_3$: A Highly Efficient Photocatalyst for Methylene Blue Degradation under Direct Sunlight,” *Ceram. Int.,* vol. 52, no. 9, Part A, pp. 12178–12191, 2026, doi: 10.1016/j.ceramint.2026.01.372.

[32] J. C. Maxwell, *A treatise on electricity and magnetism*. Oxford: Clarendon Press, 1873.

[33] K. W. Wagner, “Erklärung der dielektrischen Nachwirkungsvorgänge auf Grund Maxwellscher Vorstellungen,” *Archiv. F. Elektrotechnik*, vol. 2, pp. 371–387, Sept. 1914, doi: 10.1007/BF01657364.

[34] C. G. Koops, “On the Dispersion of Resistivity and Dielectric Constant of Some Semiconductors at Audiofrequencies,” *Phys. Rev.*, vol. 83, pp. 121–124, Jul. 1951, doi: 10.1103/Phys Rev.83.121.

[35] Y. J. Wong, J. Hassan and M. Hashim, “Solid State Sintering and Microstructural Evolution on Wide Frequency Range Dielectric Responses of Mechanically Activated $CaTiO_3$ Ceramics,” *Adv. Mater. Res.*, vol. 1107, pp. 38–44, 2015, doi: 10.4028/www.scientific.net/AMR.1107.38.

[36] Y. J. Wong *et al*., “Dielectric Properties, Impedance Analysis and Modulus Behavior of $CaTiO_3$ Ceramic Prepared by Solid State Reaction,” *J. Alloys Compd.*, vol. 595, pp. 228–234, 2014, doi: 10.1016/j.jallcom.2013.03.123.

[37] D. Kumar and P. Kour, “Investigating structural, dielectric, and ferroelectric properties of $CaTiO_3$ nano-ceramics,” *Dig. J. Nanomater. Biostruct.*, vol. 20, no. 1, pp. 149–156, 2025, doi: 10.15251/DJNB.2025.201.149.

[38] P. Ctibor, J. Kotlan, Z. Pala, J. Sedlacek, Z. Hajkova and T. M. Grygar, “Calcium titanate ($CaTiO_3$) dielectrics prepared by plasma spray and post-deposition thermal treatment,” *Mater. Res. Bull.*, vol. 72, pp. 123–132, Dec. 2015, doi: 10.1016/j.materresbull.2015.07.041.

[39] S. S. Aung, T. T. Wai, N. H. M. Thin and Z. M. Myat, “Synthesis and Characterization of Calcium Titanate ($CaTiO_3$) Powder for Photovoltaic Application,” *J. Myanmar Acad. Arts Sci.*, vol. 18, no. 2B, 2020.

[40] B. M. Patil, R. S. Srinivasa and S. R. Dharwadkar, “Synthesis of $CaTiO_3$ from calcium titanyl oxalate hexahydrate (CTO) as precursor employing microwave heating technique,” *Bull. Mater. Sci.*, vol. 30, pp. 225–229, Jun. 2007, doi: 10.1007/s12034-007-0040-7.

[41] C. Karthikeyan, M. Thamima and S. Karuppuchamy, “Structural and Photocatalytic Property of $CaTiO_3$ Nanosphere,” *MSF*, vol. 979, pp. 169–174, Mar. 2020, doi: 10.4028/www.scientific.net/msf.979.169.